High-level ab initio quartic force fields and spectroscopic characterization of C2N-

Romero Rocha, C.M.; Linnartz, H.V.J.

PCCP

ARTICLE TYPE

Cite this: DOI: 00.0000/xxxxxxxxxx

High-level ab initio quartic force fields and spectroscopic characterization of C_2N^- †

C. M. R. Rocha*[a] and H. Linnartz[a]

Received Date
Accepted Date

DOI: 00.0000/xxxxxxxxxx

While it is now well established that large carbon chain species and radiative electron attachment (REA) are key ingredients triggering interstellar anion chemistry, the role played by smaller molecular anions, for which REA appears to be an unlikely formation pathway, is as yet elusive. Advancing this research undoubtedly requires the knowledge (and modeling) of their astronomical abundances which, for the case of C_2N^-, is largely hindered by a lack of accurate spectroscopic signatures. In this work, we provide such data for both ground ℓ-CCN$^-$($^3\Sigma^-$) and low-lying c-CNC$^-$($^1A_1$) isomers and their singly-substituted isotopologues by means of state-of-the-art rovibrational quantum chemical techniques. Their quartic force fields are herein calibrated using a high-level composite energy scheme that accounts for extrapolations to both one-particle and (approximate) $\mathscr{N}$-particle basis set limits, in addition to relativistic effects, with the final forms being subsequently subject to nuclear motion calculations. Besides standard spectroscopic attributes, the full set of computed properties includes fine and hyperfine interaction constants and can be readily introduced as guesses in conventional experimental data reduction analyses through effective Hamiltonians. On the basis of benchmark calculations performed anew for a minimal test set of prototypical triatomics and limited (low-resolution) experimental data for ℓ-CCN$^-$($^3\Sigma^-$), the target accuracies are determined to be better than 0.1% of experiment for rotational constants and 0.3% for vibrational fundamentals. Apart from laboratory investigations, the results here presented are expected to also prompt future astronomical surveys on C_2N^-. To this end and using the theoretically-predicted spectroscopic constants, the rotational spectra of both ℓ-CCN$^-$($^3\Sigma^-$) and c-CNC$^-$($^1A_1$) are derived and their likely detectability in the interstellar medium is further explored in connection with working frequency ranges of powerful astronomical facilities. Our best theoretical estimate places c-CNC$^-$($^1A_1$) at about 15.3 kcal mol^{-1} above the ground-state ℓ-CCN$^-$($^3\Sigma^-$) species.

1 Introduction

The plausible existence and role of negative molecular ions in the interstellar medium (ISM) were put forward in the early days of astrochemistry by several authors[1–3]. However, while their parent cation and neutral species have soon emerged as tempting targets for radioastronomical surveys[4] and paved the way for explaining chemical synthesis in the ISM[5–9], the detection of anions remained largely elusive, particularly because of a lack of accurate rest frequencies[10]. This situation has changed recently with the laboratory and astronomical identification of the first interstellar molecular anion[11] C_6H^-. This led to a resurgence of interest of chemists, physicists, and astrophysicists in anions, motivating new surveys as well as theoretical and laboratory studies[12–15]. As a result, several other negatively charged species were soon identified like C_4H^-, C_8H^-, C_3N^-, C_5N^- and CN^- (Refs. 15, 16 and references therein).

Very early on, it has been suggested[2,3] that, under typical interstellar conditions, the formation of such anionic inventory (X^-) could be mainly ascribed to radiative electron attachment (REA) to the existing neutrals (X)[3,17–23]:

$$X + e^- \underset{k_d}{\overset{k_c}{\rightleftharpoons}} [X^-]^* \xrightarrow{k_r} X^- + h\nu. \quad (1)$$

As noted elsewhere[3,18,19,22], reaction (1) implies a competition, following electron capture (k_c), between auto-detachment (k_d) and radiative stabilization (k_r) of the initially formed (transient) superexcited complex $[X^-]^*$; in dilute astrophysical media, collisional stabilization of $[X^-]^*$ is assumed negligible[15]. Using phase-space theory (PST) and relying on the mechanism (1), Herbst[3] first derived a theoretical expression for the overall REA rate constant (k_{REA}) – the results pointed towards an interesting conclusion: k_{REA} increases greatly with increasing molecular size and

[a] Laboratory for Astrophysics, Leiden Observatory, Leiden University, P.O. Box 9513, NL-2300 RA Leiden, The Netherlands. E-mail: romerorocha@strw.leidenuniv.nl

† Electronic Supplementary Information (ESI) available. See DOI: 00.0000/00000000.

electron affinity of the target neutrals [3,18,19,22]. Moreover, for X species with large dipole moments ($\mu \gtrsim 2$-2.5 D), it has later been recognized [22,24–26] that the existence of dipole-driven resonances [25,26] and (excited) dipole-bound states [12,14,27] are key to enhance further the $[X^-]^*$'s lifetime (with respect to autodetachment), and hence the efficiency of REA. Thus, provided that the k_r's are high, such anions may be formed with sizeable rates ($k_{REA} \sim 10^{-7}\,cm^3\,s^{-1}$) and, depending on the local ISM gas pressure and radiation field, exhibit appreciable anion-to-neutral ratios [3,22]. It was for this reason that carbon chain anions were also considered possible carriers of diffuse interstellar bands. [28]

Assuming reaction (1) as the major anion formation route and using the theoretically-derived PST rates [3,18,19,22], previous anion chemical models have been successful in reproducing the observed abundances of the larger, highly-dipolar carbon-chain anions C_nH^- ($n>5$) and C_nN^- ($n>4$) in a variety of astronomical environments [15,20,21,23]. For example, Walsh *et al.* [23] determined anion-to-neutral ratios of $\sim$4%, $\sim$5% and $\sim$ 7% for C_8H^-, C_6H^- and C_5N^-, respectively, values that compare quite well with the ones observed in the dark cloud TMC-1 ($\sim$ 5%, $\sim$ 2% and $\sim$ 13%) [15,16]. These results provide further evidence in support of the REA hypothesis for such molecules. However, for the smallest anionic species (*e.g.*, CN^- and C_3N^-) for which REA to their parent neutrals are theorized to be very slow ($k_{REA} \lesssim 10^{-10}\,cm^3\,s^{-1}$), notable discrepancies have soon appeared between the modeled and observed anion-to-neutral ratios [15], suggesting that other alternative pathways might dominate their synthesis [16,29–34]. For example, the unusually high CN^- abundance observed towards the carbon-rich star IRC+10216 has been explained [31] by means of the fragmentation reactions C_n^-+N→CN^-+C_{n-1} [35]; a similar synthetic route (C_n^-+N→C_3N^-+C_{n-3}) has been later proposed to also dominate the production of C_3N^- in TMC-1 [16]. Subsequent quantum mechanical calculations by Gianturco *et al.* [33] provided compelling evidence in favor of the H^-+HC_nN reactions as additional prime sources of elemental C_nN^-'s under typical ISM conditions. Based on laboratory experiments, Chacko *et al.* [36] recently suggested a novel formation pathway for smaller interstellar C_nN^-/C_n^- species – it involves the fragmentation decay of superexcited resonance anion states of larger analogues (*e.g.*, $[C_nN^-]^*$ with $n=3,5,6,7$) that can be formed from impinging UV photons onto the external layers of IRC+10216 [see Eq. (1)]. The results pointed out the dominance of C_2^- and C_2N^- as fragmentation products, thereby offering invaluable prospects into their omnipresence in the circumstellar shells of IRC+10216 [36]. Indeed, these species are yet to be identified in space and their laboratory and theoretical characterization is tempting/timely. It should be noted that, apart from circumstellar envelopes, the conclusions drawn by Chacko *et al.* [36] are expected to also prompt future astronomical surveys on C_2^- and C_2N^- in strongly shielded environments like TMC-1, although their existence therein (if at all) must entail distinct chemical formation routes. Thus, studying the astronomical abundance of these smaller species is key to a proper understanding of a ISM anion chemistry beyond REA [31]. For this, accurate spectral features of such molecules should then be gathered. Still, while C_2^- is spectroscopically well-characterized in the laboratory (Ref. 37 and references therein), the amount of theoretical and experimental data on the carbonitrile anion C_2N^- is as yet very limited [38–41].

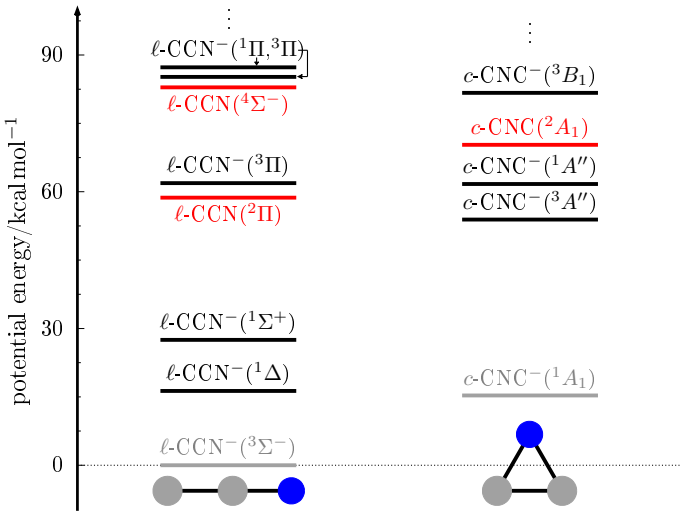

Fig. 1 Linear (ℓ-) and cyclic (c-) stationary points on the ground and some low-lying excited potential energy surfaces of C_2N. Relative energies are obtained at the MRCI(Q)/AV*T*Z//CASSCF/AV*T*Z level of theory. Red and black structures denote the corresponding neutral and anionic excited states, respectively, while the gray lines symbolize the target anion forms considered in the present study.

In light of the foregoing, this work thus aims at providing accurate rovibrational spectroscopic constants and anharmonic vibrational frequencies for C_2N^- by means of a high-level theoretical approach (see below). Indeed, its parent neutral form, ℓ-CCN($^2\Pi$), has only recently been detected in the circumstellar envelope of IRC+10216 [42]. Despite having a relatively small dipole moment ($\mu_e \approx 0.3$ D [43]), ℓ-CCN($^2\Pi$) is characterized by a high (positive) electron affinity, EA = 2.7489 ± 0.001 eV [39], hence rendering the corresponding ground-state anion, ℓ-CCN$^-$($^3\Sigma^-$), exceptionally stable with respect to electron loss [39]; see Figure 1. As in the case of C_2^- [37], this is manifested in the very existence of bound electronically excited C_2N^- states that lie below its photodetachment threshold (Figure 1) and that can be optically connected to ℓ-CCN$^-$($^3\Sigma^-$). Such a high electron binding energy, in combination with a large dipole moment ($\mu_e \approx 2.0$ D), makes ℓ-CCN$^-$($^3\Sigma^-$) amenable to observation with new powerful instruments such as the atacama large millimeter/submillimeter array (ALMA) and the Green Bank Telescope (GBT). Apart from the linear ground-state, a low-energy cyclic C_{2v} form of C_2N^-, c-CNC$^-$($^1A_1$), [lying *ca.* 15 kcal mol^{-1} above ℓ-CCN$^-$($^3\Sigma^-$)] [38] exists (Figure 1) that may be equally relevant to interstellar chemistry [40,44] and is likewise focus of the present study. Indeed, besides acyclic (small) cyano precursors [45,46], there is compelling evidence that such elemental N-heterocycles might also play a role into the chemical evolution of larger astrobiologically-relevant species [47]. In addition to interstellar and circumstellar environments, we should also mention the likely pertinence of these nitrile anions to the atmosphere of Titan wherein a rich N-based anion chemistry is known to prevail [48].

As for their theoretical spectroscopic characterization, we

herein employ the so-called quartic force field (QFF) approach[40,49–53]. Within this framework, the potential energy surfaces (PESs)[54] of ℓ-CCN$^-$($^3\Sigma^-$) and c-CNC$^-$($^1A_1$) are represented locally by fourth-order Taylor series expansions:[55]

$$V(\mathbf{R}) = \frac{1}{2}\sum_{ij} F_{ij}\Delta_i\Delta_j + \frac{1}{6}\sum_{ijk} F_{ijk}\Delta_i\Delta_j\Delta_k + \frac{1}{24}\sum_{ijkl} F_{ijkl}\Delta_i\Delta_j\Delta_k\Delta_l, \quad (2)$$

where $\mathbf{R} = \{R_1, R_2, R_3\}$ denotes an arbitrary set of internal coordinates, $\Delta_i = R_i - R_i^e$ represent coordinate displacements from the equilibrium geometries $\mathbf{R_e} = \{R_1^e, R_2^e, R_3^e\}$ and $F_{ij\ldots} = \partial^n V/\partial\Delta_i\partial\Delta_j\ldots|_{\Delta_{i,j,\ldots}=0}$ the force constants; the unrestricted summations run over all possible coordinate indices $3 \geq i,j,k,l \geq 1$. These QFFs will then be computed using highly accurate *ab initio* energies[43,49,50], with the final forms being subsequently subject to nuclear motion calculations[56–60]. The details of such a methodology are scrutinized in section 2, while the results are presented in Section 3. The astrophysical implications are briefly surveyed in Section 4, with the conclusions being gathered in Section 5

2 Theoretical methods

2.1 *Ab initio* calculations & QFFs

The full QFFs for the C_2N anions were computed by performing accurate *ab initio* calculations on equally spaced grid points centered at best-guess equilibrium structures (see below). A total of 85 symmetry-unique geometries were sampled based on a finite (central) difference approach; the step lengths taken were ± 0.005 Å/rad. In generating such grids for ℓ-CCN$^-$($^3\Sigma^-$), we have employed simple internal displacement coordinates[51], *i.e.*,

$$\Delta_1 = r(\mathrm{C_1{-}N}) - r_e(\mathrm{C{-}N}),$$
$$\Delta_2 = r(\mathrm{C_1{-}C_2}) - r_e(\mathrm{C{-}C}) \quad (3)$$

for stretches and

$$\Delta_{3,4} = \sin[\angle(\mathrm{C{-}C{-}N})] - \sin[\angle_e(\mathrm{C{-}C{-}N})] \quad (4)$$

for the degenerate linear bends; r and $\angle$ define bond lengths and angle, respectively, with the subscript e denoting the corresponding equilibrium values; see Figure 2. Note that only one component, Δ_3, was considered in the finite difference calculations; bending force constants depending on Δ_4 are herein determined via cylindrical symmetry relations[61]

$$F_{3344} = (F_{333} + 4F_{33})/3, \qquad F_{33ij} = F_{44ij},$$
$$F_{33i} = F_{44i}, \qquad F_{33} = F_{44} \qquad \forall i,j. \quad (5)$$

For c-CNC$^-$($^1A_1$), the following symmetry-internal displacement coordinates were used[52]:

$$\Delta_1 = \frac{1}{\sqrt{2}}[r(\mathrm{N{-}C_1}) + r(\mathrm{N{-}C_2}) - 2r_e(\mathrm{N{-}C})]$$
$$\Delta_2 = \angle(\mathrm{C{-}N{-}C}) - \angle_e(\mathrm{C{-}N{-}C})$$
$$\Delta_3 = \frac{1}{\sqrt{2}}[r(\mathrm{N{-}C_1}) - r(\mathrm{N{-}C_2})]. \quad (6)$$

At each selected geometry $\mathbf{R}$, the total electronic energy, E, was then obtained via a composite scheme[43,49,50]

$$E(\mathbf{R}) = E_\infty^{\mathrm{CC}}(\mathbf{R}) + \Delta_{\mathrm{DKH}}(\mathbf{R}) + \Delta_{\mathrm{HO}}(\mathbf{R}), \quad (7)$$

where E_∞^{CC} is an estimate of the one-particle complete basis set (CBS) limit[62], including core and core-valence correlation, at the coupled cluster singles and doubles level of theory with perturbative triples[63] [CCSD(T) or, briefly, CC], Δ_{DKH} is a correction for scalar relativistic effects[64], and Δ_{HO} accounts for higher-order (HO) electron correlation contributions beyond CC. All calculations have been performed at the spin-restricted (open-shell) CC level of theory[63,65,66] using the restricted (open-shell) Hartree-Fock (HF) determinant as reference. The VXZ ($X = D,T,Q,5$) basis sets of Dunning and co-workers[67] with additional diffuse[68] (AVXZ) and core correlation functions[69] (ACVXZ) were employed throughout, with the computations done with `MOLPRO`[70]. To ensure accuracy of the final force constants, all calculations have been carried out with a convergence energy criteria of $10^{-12}\,E_{\mathrm{h}}$[49,50].

Due to the distinct asymptotic convergence rates[62], the CBS extrapolations for the HF and total CC electron correlation (cor) components of E_∞^{CC} [Eq. (7)] were performed individually, *i.e.*,

$$E_\infty^{\mathrm{CC}}(\mathbf{R}) = E_\infty^{\mathrm{HF}}(\mathbf{R}) + E_\infty^{\mathrm{cor}}(\mathbf{R}). \quad (8)$$

For the HF energy, a three-point exponential-type formula has been so employed[71]

$$E_X^{\mathrm{HF}}(\mathbf{R}) = E_\infty^{\mathrm{HF}}(\mathbf{R}) + A\exp(-BX), \quad (9)$$

where E_∞^{HF}, A, and B are parameters to be calibrated from HF/ACVXZ ($X = T,Q,5$) energies. In turn, the extrapolated cor contributions are obtained via the inverse-power formula[72]

$$E_X^{\mathrm{cor}}(\mathbf{R}) = E_\infty^{\mathrm{cor}}(\mathbf{R}) + A'X^{-3} + B'X^{-5}, \quad (10)$$

where E_∞^{cor}, A' and B' are calibrated from the raw CC/ACVXZ ($X = T,Q,5$) total correlation energies.

In Eq. (7), the corrections due to scalar relativistic contributions were obtained by

$$\Delta_{\mathrm{DKH}}(\mathbf{R}) = E_{\mathrm{DKH}}(\mathbf{R}) - E_{\mathrm{NR}}(\mathbf{R}), \quad (11)$$

where E_{DKH} is the total second-order Douglas-Kroll-Hess (DKH)[64,73,74] CC energy calculated with the VTZ-DK basis set[75]; E_{NR} defines its non-relativistic CC/VTZ-DK counterpart. As for the estimation of higher-order electron correlation, Δ_{HO} [Eq. (7)], we herein include three additional (frozen-core) energy incre-

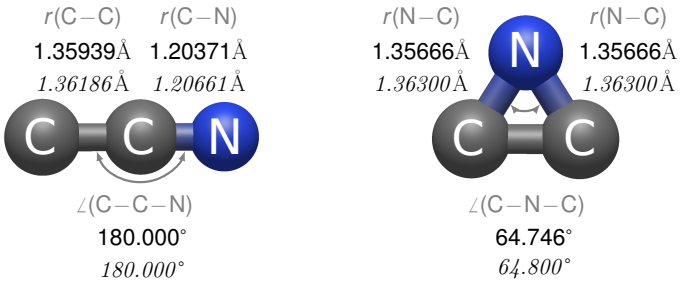

Fig. 2 Internal coordinate definitions for ℓ-CCN$^-$($^3\Sigma^-$) and c-CNC$^-$($^1A_1$). Also shown are the corresponding equilibrium (in **bold**) and vibrationally averaged structures (in *italic*) for the main isotopologues as determined from our final composite QFFs; see later Tables 2 and 3 for further details.

ments[43,76,77]

$$\Delta_{\rm HO}(\mathbf{R}) = \Delta{\rm T}(\mathbf{R}) + \Delta{\rm Q}(\mathbf{R}) + \Delta{\rm FCI}(\mathbf{R}), \qquad (12)$$

where ΔT and ΔQ account for the residual CC correlation components associated with iterative triple (T_3) and quadruple (T_4) excitations; the first is obtained via differences in energy between CCSDT[78,79] and CCSD(T) calculations with the VQZ basis set, while the second is determined from CCSDTQ[80,81]/VDZ and CCSDT/VDZ energy differences. The importance of such corrections (and cost-effective variants) for accurate predictions of spectroscopic/thermochemical properties of small-to-medium sized molecules has been emphasized in several previous works[49,53,77,82–86]. Furthermore, to account for the small, residual errors arising from the truncation of the $\mathscr{N}$-particle expansions at the CCSDTQ level, we also include in Eq. (12) an estimate of the difference in correlation energy between CCSDTQ and full configuration interaction (FCI), ΔFCI, calculated with the VDZ basis set ($X = D$). The FCI limit was then obtained via a continued fraction (cf) approximant[76,87]

$$E_X^{\rm FCI}(\mathbf{R}) \approx \frac{E_X^{\rm CCSD}}{1 - \left[\left(\frac{\delta_{\rm T}}{E_X^{\rm CCSD}}\right) \Big/ \left(1 - \frac{\delta_{\rm Q}}{\delta_{\rm T}}\right)\right]}, \qquad (13)$$

where $\delta_{\rm T} = E_X^{\rm CCSDT} - E_X^{\rm CCSD}$ and $\delta_{\rm Q} = E_X^{\rm CCSDTQ} - E_X^{\rm CCSDT}$. Thus, ΔFCI in Eq. (12) is defined as $E_X^{\rm FCI} - E_X^{\rm CCSDTQ}$. For systems with small-to-moderate multireference character [the $\mathscr{T}_1$ diagnostic values for ℓ-CCN$^-$($^3\Sigma^-$) and c-CNC$^-$($^1A_1$) are ≈0.025 and 0.012, respectively], Eq. (13) has shown to be a viable alternative for estimating electron correlation beyond CCSDTQ, recovering nearly 80% of available FCI corrections[76,77]. It should be noted, however, that, while the use of the CCSDTQP method[88] and larger basis sets, *e.g.*, VTZ, would be preferable in estimating $E_X^{\rm FCI}$ (see, *e.g.*, Ref. 77) and ΔQ, respectively, the associated computational cost would make the task of calculating the QFFs intractable with current available resources; all HO corrections have been computed with the MRCC[89] code.

Due to a lack of accurate experimental geometries for C_2N^-, the determination of the reference structures in which to expand our QFFs relied solely on high-level *ab initio* estimates[50]. This has been done by first optimizing geometries at the CC/ACVTZ level, followed by computations of cost-effective QFFs therein using CBS-extrapolated CC/ACVXZ ($X = D, T, Q$) plus $\Delta_{\rm DKH}$ energies [Eqs. (8)-(11)]. The resulting fine-tuned minima were then utilized as reference for final geometry displacements and energy evaluations via Eq. (7). Of course, as these optimum configurations are not exact minima on the final composite PESs, accurate QFFs and equilibrium geometries could only be obtained by least-squares fitting such a composite energy set to Eq. (2); the sum of squared residuals were typically $10^{-15}\,E_{\rm h}{}^2$, with the resulting force constants being numerically defined in Table 1.

Table 1 Internal coordinate force constants for the C_2N anions as determined from our final composite QFFs [Eqs. (2) and (7)]. Units are mdyn Å^{-n}rad^{-m} appropriate for an energy unit of mdyn Å(≡ aJ). Eqs. (3)-(6) define the coordinates.

	ℓ-CCN$^-$($^3\Sigma^-$)	c-CNC$^-$($^1A_1$)	
	QFF[a]	QFF[a]	QFF[b]
F_{11}	12.364302	8.601837	8.613181
F_{21}	2.083929	3.701487	3.697293
F_{22}	5.491370	6.094652	6.098824
$F_{33/44}$[c]	0.414145	5.415849	5.451568
F_{111}	−94.3113	−37.2385	−37.1905
F_{211}	2.4761	−11.6437	−11.5930
F_{221}	−6.9087	−23.3909	−23.3002
$F_{331/441}$[c]	−0.8749	−26.7040	−26.6360
F_{222}	−38.6440	−46.5351	−46.2960
$F_{332/442}$[c]	−0.4844	−2.0261	−1.9450
F_{1111}	497.67	133.99	133.55
F_{2111}	21.11	29.28	29.29
F_{2211}	−17.79	54.40	54.25
$F_{3311/4411}$[c]	−0.30	103.14	102.91
F_{2221}	16.36	119.50	118.99
$F_{3321/4421}$[c]	2.43	−18.96	−18.22
F_{2222}	207.87	316.24	313.96
$F_{3322/4422}$[c]	−0.75	−41.59	−40.55
$F_{3333/4444}$[c]	2.16	74.07	73.89
F_{3344}[c]	1.27		

[a] This work.
[b] Ref. 40.
[c] Only relevant for ℓ-CCN$^-$; see Eq. (5).

2.2 (Ro)Vibrational calculations and spectroscopic constants

With such QFFs at hand, the correspoding rovibrational energy levels and associated spectroscopic constants can then be determined by solving the nuclear Schrödinger equation (NSE)[54]. This has been here accomplished through standard second-order perturbation theory (VPT2)[56–58] as implemented in SPECTRO[60]. As usual[40,52], SPECTRO requires the input of the appropriate resonances; for ℓ-CCN$^-$($^3\Sigma^-$), they correspond to Fermi type-1 ($2\nu_2 \approx \nu_3$), while type-C Coriolis ($\nu_2 \approx \nu_3$) and Darling-Dennison ($2\nu_2 \approx 2\nu_3$) resonances are input for c-CNC$^-$($^1A_1$). Besides VPT2, rovibrational band origins were also obtained using the exact kinetic energy nuclear motion code DVR3D[59] which computes variationally exact solutions to the three-atom NSE within the framework of the discrete variable representation[59]; sample SPECTRO

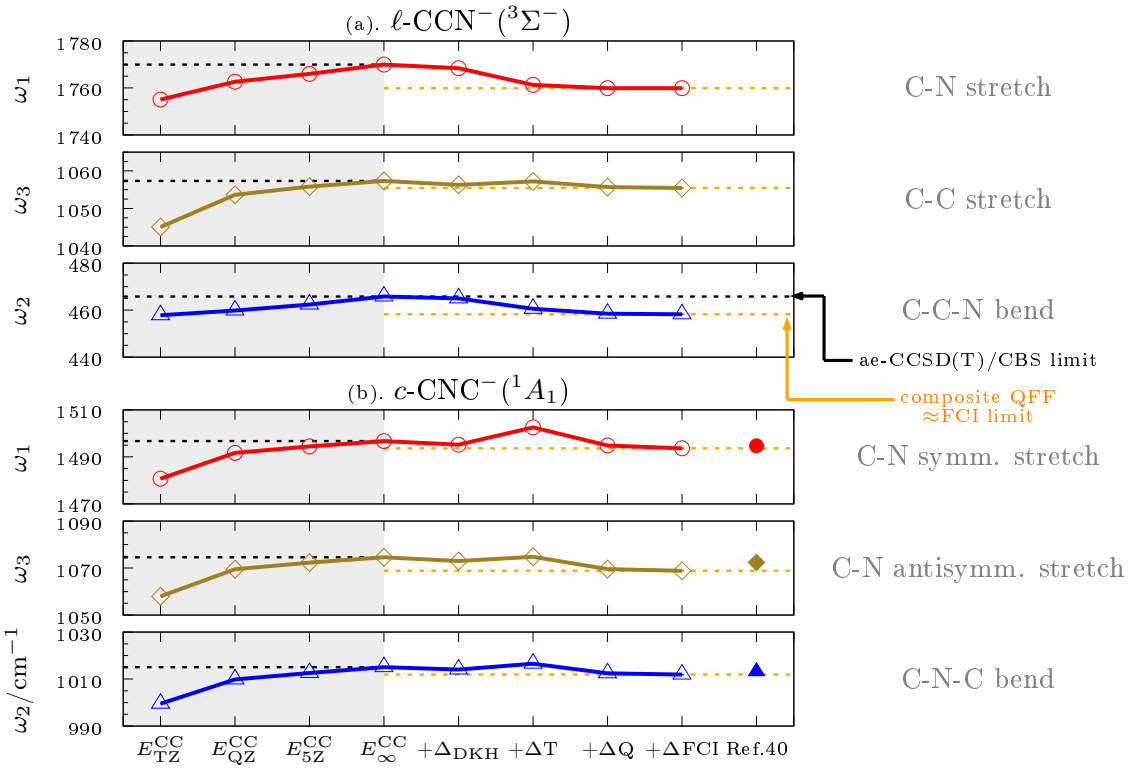

Fig. 3 Convergence of the predicted harmonic frequencies (in cm^{-1}) for (a). ℓ-$CCN^-(^3\Sigma^-)$ and (b). c-$CNC^-(^1A_1)$ as a function of each energy increment in Eq. (7). For comparison, we also show the calculated values from the raw CC/ACVXZ ($X=T,Q,5$) QFFs separately as well as the most accurate results from the literature[40] for the c-CNC^- species [panel (b)]. Shaded gray areas mark the transition region from one-particle to $\mathcal{N}$-particle expansion extrapolations. Black and orange lines outline the corresponding frequencies obtained at the one-particle CBS limit (E_∞^{CC}) and from the final QFFs, respectively; ae stands for all electron (non-frozen-core) values.

inputs and the parameters employed in DVR3D are given in the Electronic Supplementary Information (ESI). Note that, to avoid non-physical results and ensure the correct limiting behavior of the PESs, the QFFs of ℓ-$CCN^-(^3\Sigma^-)$ and c-$CNC^-(^1A_1)$ have been analytically transformed into Morse-sine and Morse-cosine coordinate representations, respectively, prior to the variational DVR3D calculations (VAR); the reader is addressed to Refs. 90 and 91 for further details.

2.3 Benchmark calculations

To assess the performance of the above protocol, preliminary benchmark calculations have been carried out for a limited set of triatomics for which accurate gas-phase experimental data are available. The selected targets comprise the prototypical ℓ-$HCN(^1\Sigma^+)$ and c-$H_2O(^1A_1)$ molecules as well as ℓ-$CCO(^3\Sigma^-)$, an open-shell species that is isoelectronic to C_2N^-, hence expected to show a similar electronic structure; the final force constants and detailed data analysis are presented in Tables S2-S4. The results indicate that our present methodology is capable of producing vibrationally-averaged rotational constants and vibrational fundamentals to within $\sim$0.1% (22 MHz) and $\sim$0.3% (3 cm^{-1}) of experiment, respectively, for species with at least two heavy atoms, hence further showcasing its reliability. This is about the accuracy one might expect for the predicted spectroscopic attributes of ℓ-$CCN^-(^3\Sigma^-)$ and c-$CNC^-(^1A_1)$ and is quite consistent with well-established state-of-the-art QFF/VPT2 protocols currently available in the literature[49,53,86,92].

3 Results

Figure 3 displays the dependence of the ℓ-$CCN^-(^3\Sigma^-)$ and c-$CNC^-(^1A_1)$ harmonic frequencies for the three fundamental modes (ω_i) on the ACVXZ basis set size at the CC level as well as upon inclusion of the Δ_{DKH} [Eq. (11)] and Δ_{HO} [Eq. (12)] energy increments [Eq. (7)]; the corresponding profiles obtained for equilibrium geometries (R_i^e) are depicted in Figure S1 (see also Figure 2 to assess their final values). Tables 2-6 gather the calculated rovibrational spectroscopic constants, vibrational fundamentals and anharmonic constants for the various C_2N^- forms as obtained from our final composite QFFs and VPT2/VAR. Note that, apart from the main isotopologues, detailed spectroscopic data are also presented for the ^{13}C and ^{15}N singly-substituted species.

3.1 Effects of various corrections on equilibrium properties

A close inspection of Figure 3 unravels the slow convergence rates of the raw CC/ACVXZ ($X=T,Q,5$) harmonic frequencies towards the predicted CBS values, a feature clearly expected from standard all electron (ae) CC methods[82]; see shaded gray areas and the black dashed lines outlined therein. A similar convergence behavior is also found for the R_i^e's (Figure S1). In-

Table 2 Equilibrium structures and spectroscopic vibration-rotation constants of ℓ-CCN$^-$($^3\Sigma^-$) isotopologues. Data determined from our final composite QFF (Table 1) via second-order perturbation theory (VPT2)[56–58]. The bottom part gathers the *ab initio* calculated fine and leading hyperfine interaction constants at the QFF equilibrium geometry. Units are MHz unless stated otherwise.

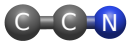	ℓ-CCN$^-$	ℓ-^{13}CCN$^-$	ℓ-C^{13}CN$^-$	ℓ-CC^{15}N$^-$
	QFF[a]	QFF[a]	QFF[a]	QFF[a]
r_0(C−C)/pm	136.1860	136.1765	136.1882	136.1839
r_0(C−N)/pm	120.6613	120.6565	120.6562	120.6600
$\angle_0$(C−C−N)/°	180.0000	180.0000	180.0000	180.0000
B_0	11 861.91	11 369.30	11 862.02	11 490.06
B_1	11 796.21	11 307.99	11 800.31	11 423.77
B_2	11 893.37	11 399.60	11 891.87	11 520.70
B_3	11 795.79	11 309.84	11 791.59	11 429.12
$10^3 D_e$	6.130	5.692	6.128	5.700
$10^6 H_e$	−0.002	−0.002	−0.002	−0.002
q	−28.489	−26.346	−29.257	−26.867
α_1^B	65.7	61.3	61.7	66.3
α_2^B	−31.5	−30.3	−29.8	−30.6
α_3^B	80.2	76.3	80.7	75.2
r_e(C−C)/pm	135.9387	-	-	-
r_e(C−N)/pm	120.3706	-	-	-
$\angle_e$(C−C−N)/°	180.0000	-	-	-
B_e	11 903.44	11 407.80	11 903.38	11 530.17
μ_e/D[b]	1.9873	1.8190	1.9869	2.1347
λ_e[c]	11 958.87	-	-	-
γ_e[c]	−19.16	−18.37	−19.16	−18.56
$b_F(^{14}\mathrm{N})$[d]	19.84	19.84(65.03)	19.84(−49.72)	-
$c(^{14}\mathrm{N})$[d]	−16.24	−16.24(−56.62)	−16.24(15.80)	-
$eQq(^{14}\mathrm{N})$[e]	−2.9088	-	-	
$\eta(^{14}\mathrm{N})$[e]	0.0000	-	-	

[a] This work. Data obtained using SPECTRO[60]. Rotational constants (B_i), vibration-rotation interaction constants (α_i^B), quartic (D_e) and sextic (H_e) centrifugal distortion parameters and ℓ-type doubling constant (q) are all in MHz. B_i with i=1-3 are effective rotational constants calculated for the three vibrational fundamentals; see Figure 3 for mode descriptions. The corresponding zero-point level constant is B_0.

[b] CBS-extrapolated dipole moments (in D) at the QFF equilibrium geometry; see Ref. 93.

[c] Spin-spin (λ_e) and spin-rotation (γ_e) coupling constants (in MHz); see text.

[d] Electron spin-nuclear spin hyperfine coupling constants. Isotropic Fermi-contact (b_F) and anisotropic dipole-dipole (c) magnetic couplings (both in MHz) evaluated at the ^{14}N nucleus. The corresponding values obtained at ^{13}C are given in parenthesis; couplings at ^{15}N are not explicitly considered.

[e] CBS-extrapolated ^{14}N nuclear quadrupole (hyperfine) coupling constant (eQq in MHz) and asymmetry parameter (η unitless); see text.

deed, on going from the smaller ACV*T*Z to the ACV5Z basis set, the predicted CCSD(T) equilibrium bond distances decrease by $\approx$0.01 Å, followed by increments of $\approx 10\,\mathrm{cm}^{-1}$ in the corresponding harmonic frequencies. In turn, extrapolations to the CBS limit produce only minor changes in the CC/ACV5Z attributes, as expected: the ω_i's and R_i^e's vary by less than $+2\,\mathrm{cm}^{-1}$ and -0.002 Å/-0.005 deg, respectively. Moreover, the inclusion of scalar relativity [Δ_{DKH} in Eq. (11)] into E_∞^{CC} [Eqs. (8)-(10)] leads to only slight, but still significant reductions in both ω_i and R_i^e. As expected for such light molecules, these corrections are small and amount to $\approx -62\,\mathrm{mE_h}$ around equilibrium. In addition to the one-particle basis set correlation recovery at CC, Figures 3 and S1 also permit an approximate assessment of the ω_i and R_i^e convergence rates upon increasing coupled cluster $\mathcal{N}$-particle expansions [CCSD(T)→CCSDT→CCSDTQ⟶≈FCI]; see white regions and orange dashed lines. When added to the $E_\infty^{\mathrm{CC}}+\Delta_{\mathrm{DKH}}$ components, the CCSDT corrections to CCSD(T), ΔT in Eq. (12), are shown to slightly overestimate (underestimate) the bond angle (bond distances) of c-CNC$^-$($^1A_1$), thus leading to a net increase in the ω_i's; the contrary is the case for the linear species. Indeed, the ΔT correlation contributions to the total energies assume opposing signs for c-CNC$^-$($^1A_1$) and ℓ-CCN$^-$($^3\Sigma^-$), being of the order of $+0.6$ and $-1\,\mathrm{mE_h}$, respectively. Yet, faster convergence rates of these equilibrium properties towards their (approximate) FCI limit values are clearly perceived after the addition of the correlation component due to iterative quadruples, ΔQ [Eq. (12)]. As noted elsewhere[77,83,85], the weaker dependence on the basis set size and the increasingly faster convergence rates of the HO terms (notably, ΔQ and corrections beyond it) are demonstrably attributed to their intimate relation to non-dynamical rather than dynamical correlation. In fact, at the CCSDTQ level, the predicted equilibrium geometries and harmonic

Table 3 Equilibrium structures, A-reduced Hamiltonian spectroscopic constants (in the I^r representation), and vibration-rotation interaction constants of c-CNC$^-$($^1A_1$) isotopologues. Data determined from our final composite QFF (Table 1) via second-order perturbation theory (VPT2)[56–58]. The bottom part gathers the *ab initio* calculated leading hyperfine interaction constants at the QFF equilibrium geometry. Units are MHz unless stated otherwise.

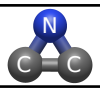	c-CNC$^-$		c-^{13}CNC$^-$		c-C^{15}NC$^-$	
	QFF[a]	QFF[b]	QFF[a]	QFF[b]	QFF[a]	QFF[b]
r_0(N−C)/pm	136.3000	136.2734	136.2858 136.3007	136.2593	136.2903	136.2637
$\angle_0$(C−N−C)/°	64.800	64.812	64.796	64.808	64.804	64.816
A_0	43384.08	43406.38	42962.76	42983.82	41567.27	41588.32
B_0	39690.76	39692.55	37968.13	37970.92	39690.61	39692.89
C_0	20644.40	20650.27	20075.91	20081.47	20222.86	20228.62
A_1	43112.40	43135.49	42683.37	42705.39	41323.55	41345.21
B_1	39544.95	39548.05	37843.00	37846.70	39532.99	39536.49
C_1	20543.71	20550.14	19980.79	19986.89	20123.93	20130.19
A_2	43682.21	43702.28	43226.36	43245.79	41841.29	41860.34
B_2	39316.60	39322.04	37639.10	37644.64	39329.04	39334.66
C_2	20526.23	20532.55	19960.63	19966.63	20111.50	20117.66
A_3	43068.78	43092.86	42682.84	42705.30	41268.88	41291.64
B_3	39775.85	39778.95	38023.34	38027.50	39774.62	39777.98
C_3	20512.25	20519.05	19949.32	19955.76	20093.81	20100.50
$10^3\Delta_J$	117.187	117.065	106.299	106.161	116.772	116.650
$10^3\Delta_{JK}$	−80.725	−81.807	−56.421	−57.192	−90.260	−91.279
$10^3\Delta_K$	206.300	207.050	186.291	186.687	196.297	197.022
$10^3\delta_J$	49.439	49.381	44.453	44.386	49.647	49.589
$10^3\delta_K$	86.773	86.145	90.374	89.849	76.408	75.819
$10^6\Phi_J$	0.091	0.101	0.214	0.219	0.091	0.101
$10^6\Phi_{JK}$	5.884	5.802	2.367	2.370	5.475	5.395
$10^6\Phi_{KJ}$	−23.461	−23.196	−12.098	−12.081	−21.689	−21.439
$10^6\Phi_K$	19.839	19.635	11.194	11.172	18.191	18.002
$10^6\phi_J$	0.044	0.049	0.106	0.108	0.044	0.049
$10^6\phi_{JK}$	2.240	2.216	0.780	0.790	2.104	2.080
$10^6\phi_K$	−0.384	−0.341	2.431	2.410	−0.749	−0.706
α_1^A	271.7		279.4		243.7	
α_2^A	−298.1		−263.6		−274.0	
α_3^A	315.3		279.9		298.4	
α_1^B	145.8		125.1		157.6	
α_2^B	374.2		329.0		361.6	
α_3^B	−85.1		−55.2		−84.0	
α_1^C	100.7		95.1		98.9	
α_2^C	118.2		115.3		111.4	
α_3^C	132.2		126.6		129.0	
r_e(N−C)/pm	135.6664	135.6422	-	-	-	-
$\angle_e$(C−N−C)/°	64.746	64.759	-	-	-	-
A_e	43528.50	43550.61	43110.62	43131.31	41701.32	41722.20
B_e	39908.19	39907.41	38167.60	38167.89	39908.19	39907.66
C_e	20819.90	20824.75	20244.40	20249.04	20392.53	20397.38
μ_e/D[c]	1.1011	1.10	1.0536		1.1908	
$eQq(^{14}\mathrm{N})$[d]	5.0986		-			
$\eta(^{14}\mathrm{N})$[d]	0.0385		-			

[a] This work. Data obtained using SPECTRO[60]. Rotational constants (A_i, B_i, C_i), vibration-rotation interaction constants (α_i^A, α_i^B, α_i^C), quartic (Δ_J, Δ_{JK}, Δ_K, δ_J, δ_K) and sextic (Φ_J, Φ_{JK}, Φ_{KJ}, Φ_K, ϕ_J, ϕ_{JK}, ϕ_K) centrifugal distortion parameters are all in MHz. A_i, B_i, C_i with i = 1-3 are effective rotational constants calculated for the three vibrational fundamentals; see Figure 3 for mode descriptions. The corresponding zero-point level constants are A_0, B_0, C_0.

[b] Ref. 40.

[c] CBS-extrapolated dipole moments (in D) at the QFF equilibrium geometry; see Ref. 93.

[d] CBS-extrapolated ^{14}N nuclear quadrupole (hyperfine) coupling constant (eQq in MHz) and asymmetry parameter (η unitless) at the QFF equilibrium geometry; see text.

frequencies appear to be well converged for both species, with the inclusion of the ΔFCI [Eqs. (12) and (13)] terms being responsible for less than 0.0001 Å/−0.005 deg and $-1\,\mathrm{cm}^{-1}$ adjustments, respectively; see Figures 3 and S1. As expected, ΔQ is the largest among all HO corrections, amounting to $\approx -1.5\,\mathrm{mE_h}$; ΔFCI is of the order of $-0.1\,\mathrm{mE_h}$. To gauge the reliability of our predicted ΔFCI corrections to CCSDTQ, we have followed Ref. 77 and for comparison estimated this limit at the QFF equilibrium geometries with the cf approximant [Eq. (13)] but using instead the CCSDT/V*D*Z, CCSDTQ/V*D*Z, and CCSDTQP/V*D*Z higher hierarchical sequence; the final FCI corrections obtained in this way include additional Δ*P* terms and are thereafter denoted as $\Delta\mathrm{FCI_{true}}$. The results have shown that our "cost-effective" cf protocol based on the CCSD→CCSDT→CCSDTQ sequence series recovers nearly 80% of the "true" residual FCI correlation energies [*i.e.*, $\Delta\mathrm{FCI}/\Delta\mathrm{FCI_{true}} \approx 0.75$ and 0.8 for ℓ-CCN$^-$($^3\Sigma^-$) and *c*-CNC$^-$($^1A_1$), respectively], hence confirming its feasibility and accuracy. Similar conclusions were drawn in previous studies[76,77]. It should be emphasized that, although specialized extrapolation formulas have recently been developed for HO terms[85], no attempts have here been made to estimate these corrections at the CBS limit as this would imply a formidable computational effort. Thus, small additional (residual) one-particle basis set truncation errors may still be foreseen in our protocol, albeit with conceivably little impact on the final results. Of course, the magnitude of these uncertainties is expected to exceed those effects associated with diagonal Born-Oppenheimer (DBOC) and non-adiabatic corrections[94], and we therefore opted not to include them either in our approach. Note that a high-level QFF already exists in the literature for *c*-CNC$^-$($^1A_1$)[40]. It is based on the well-established CcCR protocol which includes, in addition to CBS-extrapolated CC/AV*X*Z ($X = T, Q, 5$) energies, core-valence and relativistic effects[14,50,51,92]. For comparison, we also plot in Figures 3 (b) and S1 (b) the predicted CcCR equilibrium properties taken from Ref. 40. Accordingly, the CcCR results agree quite well with our predicted attributes, notably when compared with the $E_\infty^{\mathrm{CC}}+\Delta_{\mathrm{DKH}}$ PES (as expected). This provides further evidence on the reliability of our CBS extrapolation protocol [Eqs. (8)-(10)]. Yet, the small discrepancies found for R_i^e and ω_i ($\approx$0.0002 Å/0.01 deg and $\lesssim 4\,\mathrm{cm}^{-1}$) are clearly attributed to the effects of HO correlations; see Tables 1, 3 , 5 and later discussions for further comparisons. Unfortunately, no experimental data is yet available for this species. This is due to the combined fact that C_2N^- molecules are not easy to produce in larger amounts and may be spectroscopically hard to identify without guiding theoretical predictions.

3.2 Molecular structures and rotational constants

As Table 2 shows, the computed C−C and C−N equilibrium bond distances for ℓ-CCN$^-$($^3\Sigma^-$) using our final composite PES are 1.359387 and 1.203706 Å, respectively. This structure is fairly close to the best-guess initial geometry (1.359176 and 1.201802 Å) utilized in the generation of the QFF *ab initio* grid points (section 2.1). To the best of our knowledge, available literature data on the ℓ-CCN$^-$($^3\Sigma^-$) equilibrium attributes is somewhat limited to the *ab initio* B3LYP studies by Pascoli[38] and Garand *et al.*[39] who reported $r_e(\mathrm{C-C})/r_e(\mathrm{C-N}) = 1.344\,\text{Å}/1.207\,\text{Å}$. Recent MRCI(Q)/AV*Q*Z calculations by Franz *et al.*[41] put better constraints on these values (1.360 and 1.212 Å). Indeed, our predicted equilibrium rotational constant, B_e, of 11903.44 MHz for the main isotopologue is ≈1% lower and greater than the corresponding DFT[38,39] (12015.49 MHz) and MRCI[41] (11820.70 MHz) values, respectively, and is expected to be the most reliable theoretical estimate currently available. With inclusion of vibrational (zero-point level) corrections via the VPT2-based α_i^B's, B_e is found to decrease by 41.52 MHz ($B_0 = 11861.91$ MHz), consistent with an increase in the vibrationally-averaged r_0 bond distances; similar trends follow for the linear rare isotopologues (Table 2). Note that, for ℓ-^{13}CCN$^-$ and ℓ-CC^{15}N$^-$, the calculated B_0 constants, 11369.30 and 11490.06 MHz, show large isotopic shifts (as expected), being ≈430 MHz smaller on average than the predicted B_0 for ℓ-CCN$^-$. Thus, differently from ℓ-C^{13}CN$^-$ (see Table 2), their pure rotational spectra should be clearly distinguished from that of the main isotopologue. Also quoted in Table 2 are the associated effective rotational constants for the three vibrational fundamentals, B_i (i=1-3); see also Figure 3 for mode descriptions.

The corresponding spectroscopic attributes obtained for *c*-CNC$^-$($^1A_1$) using our best composite QFF and VPT2 are presented in Table 3, wherein the most accurate results from the literature[40] are also listed for comparison. Accordingly, the predicted equilibrium N−C bond distance and C−N−C angle are 1.356664 Å and 64.746°, respectively. Again, these values are quite close (as expected) to the ones employed as starting reference geometry (1.355716 Å and 64.789°) and to those reported from the CcCR QFF (1.356422 Å and 64.759°)[40]. As clearly perceived from Table 3, *c*-CNC$^-$($^1A_1$) is representative of a (near-oblate) asymmetric top with $A_e = 43528.50$, $B_e = 39908.19$ and $C_e = 20819.90$ MHz, values that differ by less than 0.05% from those predicted by the CcCR protocol[40]; the largest discrepancy (of up to ∼20 MHz) is found for A_e as this appears to be the most sensitive to electron correlation[92]. Using the effective rotational constants for the zero-point level (A_0, B_0, and C_0), the calculated Ray's asymmetry parameters[95,96], κ, for the main isotopologue are thus 0.675 (this work) and 0.674 (CcCR), hence further suggesting the nearly statistical equivalence of these two theoretical data sets. The corresponding κ values calculated here for *c*-^{13}CNC$^-$ and *c*-C^{15}NC$^-$ are 0.563 and 0.824, respectively. So, as expected, substitution by ^{13}C or ^{15}N makes the corresponding ground-state vibrationally-averaged structures deviate further from or even closer to the oblate symmetric top limit ($\kappa = +1$[95,96]), respectively. As in the case of the linear form, clear differences should then be apparent in the pure rotational spectra of *c*-CNC$^-$ and its rare isotopologues. For all these species and for future reference, we also collect in Table 3 the theoretically-predicted effective rotational constants for the three vibrational fundamentals, A_i, B_i, and C_i with i=1-3.

Also listed in Tables 2 and 3 are the calculated dipole moments, μ_e, at the QFF equilibrium geometries for the various isotopologues; these were obtained using CC/ACV*X*Z ($X = Q, 5$) energies and the CBS extrapolation protocol of Ref. 93. Note that, with the exception of *c*-^{13}CNC$^-$, all dipoles are oriented along the neg-

Table 4 Calculated harmonic and anharmonic vibrational frequencies (in cm^{-1}) for ℓ-$CCN^-(^3\Sigma^-)$ isotopologues using our final composite QFF (Table 1) and SPECTRO/DVR3D.

Molecule	Description	Mode	Harmonic	VPT2[a]	VAR[b]
ℓ-CCN^-	σC−N stretch	ν_1	1759.9	1695.6	1696.5
	πC−C−N bend	ν_2	458.3	451.9	452.1
					452.9±2.9[c]
	σC−C stretch	ν_3	1055.5	1046.9	1045.8
	zero-point energy	ZPE	1866.0	1851.0	1850.3
ℓ-$^{13}CCN^-$		ν_1	1759.4	1694.6	1695.6
		ν_2	455.6	449.4	449.6
		ν_3	1027.5	1021.7	1020.6
		ZPE	1849.1	1834.2	1833.6
ℓ-$C^{13}CN^-$		ν_1	1719.4	1659.1	1659.9
		ν_2	446.1	440.0	440.2
		ν_3	1051.4	1040.1	1039.2
		ZPE	1831.5	1817.1	1816.4
ℓ-$CC^{15}N^-$		ν_1	1736.5	1673.2	1674.2
		ν_2	455.8	449.5	449.7
		ν_3	1047.0	1039.5	1038.4
		ZPE	1847.6	1832.8	1832.2

[a] This work. Data obtained using SPECTRO[60] and the internal-coordinate force field.
[b] This work. Data obtained using the variational (VAR), exact kinetic energy nuclear motion code DVR3D[59] and the QFF transformed into a Morse-sine coordinate system.
[c] Experimental value derived from Refs. 39 and 97.

ative z-axis, with the negative charge located on the N atom; the corresponding origins lie at the isotopologues' center-of-mass. Indeed, the large μ_e values so found, particularly for the linear forms ($\approx$2.0 D), indicate that these anions might be fairly bright for GBT and ALMA (see later section 4), provided the abundance of a particular isotopologue is large enough to be detectable.

3.3 (Hyper)fine splittings

To aid in future high-resolution laboratory investigations on C_2N^-, we also provide in Tables 2 and 3 reliable estimates of fine and hyperfine coupling constants[98]; see also Table S5. For ℓ-$CCN^-(^3\Sigma^-)$, the calculation of the relevant spin-spin coupling at the QFF equilibrium geometry, $\lambda_e = \lambda^e_{SO} + \lambda^e_{SS}$, followed the formalism of Vahtras *et al.*[99] where λ^e_{SO} is the contribution due to second-order spin-orbit (SO) effects, while λ^e_{SS} describes the magnetic dipole-dipole (electron) spin-spin (SS) interactions[99]. In turn, the estimation of the (electron) spin-rotation coupling constant (γ_e) relied solely[100] on its approximate relation to the electronic g-tensor as derived by Curl[101], $\gamma_e = -2B_e\Delta g_\perp$, where $\Delta g_\perp$ is the transversal component of the calculated g-shift[102] and B_e the rotational constant; all such fine structure attributes were herein obtained at the full-valence CASSCF/AVQZ level of theory using DALTON software suite[103]. To assess the reliability of such an approach, we have applied it to the isoelectronic ℓ-$CCO(^3\Sigma^-)$ species for which accurate experimental λ_0 and γ_0 values are available[104]. The calculated constants, $\lambda_e = 11594.05$ MHz and $\gamma_e = -15.04$ MHz, are in excellent agreement with the observed values[104], 11600 and −17.82 MHz, and this is the accuracy one might expect for ℓ-$CCN^-(^3\Sigma^-)$; note here the expectedly small dependence of λ and γ on zero-point vibrational corrections[104,105]. As noted previously for $O_2(^3\Sigma_g^-)$[99], ℓ-$CCO(^3\Sigma^-)$[104] and actually the case here, $\lambda_{e/0}$ is of the order of $B_{e/0}$; see Table 2.

The (hyperfine) interaction between the ^{14}N electric quadrupole moment [$Q(^{14}N) = 0.02044$ barn[106]] and the molecular electric field gradient at ^{14}N (EFG with principal-axis components $|\mathcal{V}_{zz}(^{14}N)| > |\mathcal{V}_{yy}(^{14}N)| > |\mathcal{V}_{xx}(^{14}N)|$) is herein defined by two additional parameters: the nuclear quadrupole coupling constant, $eQq(^{14}N) \propto Q(^{14}N)\mathcal{V}_{zz}(^{14}N)$, and the asymmetry parameter, $\eta(^{14}N) = [\mathcal{V}_{xx}(^{14}N) - \mathcal{V}_{yy}(^{14}N)]/\mathcal{V}_{zz}(^{14}N)$[107–109]; see Tables 2 and 3. Note that, similarly to μ_e, the relevant EFG tensors have been computed via finite field calculations in MOLPRO, with the corresponding CC/ACVXZ ($X = Q,5$) raw energies being likewise extrapolated to the CBS limit prior to the energy derivative evaluations[93]. Again, for benchmark purposes, ^{14}N hyperfine parameters were derived for the parent $CN^-(^1\Sigma)$ and ℓ-$C_3N^-(^1\Sigma)$ species using the above protocol and compared with available experimental data[110,111]. The calculated (observed) $eQq(^{14}N)$'s are −4.265 MHz (−4.238 ± 0.032 MHz[110]) and −3.253 MHz (−3.248 ± 0.005 MHz[111]), respectively; our theoretical values for ℓ-$CCN^-(^3\Sigma^-)$ and c-$CNC^-(^1A_1)$ are −2.909 and 5.099 MHz. Note that, for ℓ-$CCN^-(^3\Sigma^-)$, an additional effect arises due to the intrinsic magnetic (hyperfine) interactions between nuclei with nonzero spin (*e.g.*, ^{14}N, ^{15}N, ^{13}C) and the spin of the unpaired electrons. Such an electron spin-nuclear spin coupling has been shown to dominate the observed hyperfine structure of small open-shell Σ species[112]. The corresponding magnetic hyperfine parameters, *i.e.*, the isotropic Fermi contact (b_F) and anisotropic spin dipolar (c) interaction constants[112], at specific nucleus are listed in Table 2; these were computed at the full-valence CASSCF/ACV5Z level in DALTON[103]. Suffice it to add that, for both ℓ-$CCN^-(^3\Sigma^-)$ and c-$CNC^-(^1A_1)$, the contributions of other magnetic coupling tensors, *e.g.*, nuclear spin-rotation, amount to only a few kHz; for completeness, they are gathered in Table S5. As emphasized later in section 4, the consideration of all such (hyper)fine structure provides an additional spectroscopic identity to C_2N^- that might be fairly handy for its unambiguous detection.

3.4 Fundamental vibrational frequencies

Tables 4 and 5 report the fundamental vibrational frequencies of ℓ-$CCN^-(^3\Sigma^-)$ and c-$CNC^-(^1A_1)$ computed with VPT2/VAR and the composite force fields. Also shown for comparison are the corresponding harmonic frequencies and available results from the literature[39,40]. As seen, the agreement between VPT2 and exact variational calculations is excellent, with differences being less than 3 cm^{-1}. This is not surprising given the absence of large-amplitude fundamental modes and the existence of moderate mode-mode couplings (Table 6), features that clearly justify a VPT2 treatment[56–58]. Yet, as noted elsewhere[91], discrepancies between VPT2 and VAR may quickly appear for overtones and combination bands as their energy levels and associated wavefunctions naturally sample larger sections of the molecular PESs that may not be properly described by internal-coordinate QFFs and perturbation theory. In this context, the use of variational approaches in conjunction with Morse-cosine (-sine) PESs/QFFs becomes even more critical[91].

As Tables 4 and 5 show, the computed VPT2 anharmonic zero-

Table 5 Calculated harmonic and anharmonic vibrational frequencies (in cm^{-1}) for c-$CNC^-(^1A_1)$ isotopologues using our final composite QFF (Table 1) and SPECTRO/DVR3D.

Molecule	Description	Mode	Harmonic	VPT2[a]	VPT2[b]	VAR[c]
c-CNC^-	a_1 C−N symm. stretch	ν_1	1493.7	1461.5	1462.9	1460.3
	a_1 C−N−C bend	ν_2	1011.9	990.2	991.7	993.6
	b_2 C−N antisymm. stretch	ν_3	1068.8	1045.5	1049.4	1046.4
	zero-point energy	ZPE	1787.2	1777.5	1780.6	1778.1
c-$^{13}CNC^-$		ν_1	1476.1	1444.7	1446.2	1443.5
		ν_2	997.1	976.0	977.5	979.3
		ν_3	1054.3	1031.6	1035.5	1032.5
		ZPE	1763.8	1754.3	1757.4	1754.9
c-$C^{15}NC^-$		ν_1	1475.1	1443.6	1445.0	1442.6
		ν_2	1002.9	981.6	983.1	984.9
		ν_3	1057.0	1034.3	1038.1	1035.2
		ZPE	1767.5	1758.0	1761.1	1758.6

[a] This work. Data obtained using SPECTRO[60] and the internal-coordinate force field.
[b] Ref. 40.
[c] This work. Data obtained using the variational (VAR), exact kinetic energy nuclear motion code DVR3D[59] and the QFF transformed into a Morse-cosine coordinate system.

Table 6 Anharmonic constants (in cm^{-1}) of ℓ-$CCN^-(^3\Sigma^-)$ and c-$CNC^-(^1A_1)$ isotopologues. [a]

	ℓ-CCN^-	ℓ-$^{13}CCN^-$	ℓ-$C^{13}CN^-$	ℓ-$CC^{15}N^-$	c-CNC^-	c-$^{13}CNC^-$	c-$C^{15}NC^-$
x_{11}	−27.000	−27.016	−25.866	−26.135	−5.225	−5.200	−5.015
x_{12}	−10.483	−10.371	−9.675	−10.585	−16.993	−16.125	−17.421
x_{13}	0.277	−0.783	2.233	−0.850	−26.525	−25.918	−25.574
x_{22}	0.996	0.954	0.910	1.042	−4.757	−4.752	−4.443
x_{23}	−7.004	−6.735	−6.832	−6.912	−7.369	−6.984	−7.473
x_{33}	−8.489	−7.724	−8.986	−8.068	−3.193	−3.134	−3.126
g_{22}	−0.623	−0.582	−0.557	−0.674			

[a] This work. Data determined from our final composite internal-coordinate QFFs (Table 1) using second-order perturbation theory[56–58] as implemented in SPECTRO[60].

point energies (ZPEs) for ℓ-$CCN^-(^3\Sigma^-)$ and c-$CNC^-(^1A_1)$ are 1851.0 and 1777.5 cm^{-1}, respectively. With these values and considering the electronic energies we obtain at the corresponding QFF minima (−130.914535769027 E_h and −130.889856789944 E_h for the linear and cyclic forms), an accurate estimate of their 0 K energy difference can then be cast, this being 15.3 kcal mol^{-1} as previouly indicated (note that the use of the associated VAR ZPEs has little effect on this final value). As expected, isotopic substitution for the heavier ^{15}N or ^{13}C atoms leads to significant reductions in the isotopologues' ZPE content[114]. This is particularly true for ℓ-$C^{13}CN^-$ whose ZPE decreases by $\approx$ 34 cm^{-1} upon ^{13}C replacement; similar isotopic shifts follow for other vibrational levels.

According to Table 4, our best (variational) results for the ℓ-$CCN^-(^3\Sigma^-)$ fundamentals are 1696.5 (ν_1), 452.1 (ν_2), and 1045.8 cm^{-1} (ν_3). Most evidently, the calculated VPT2 and VAR ν_2 (C−C−N bend) frequencies are shown to match nearly perfectly the corresponding experimental estimate of[39,97] 452.9 ± 2.9 cm^{-1}, exhibiting errors of only $\lesssim$ 1 cm^{-1}; see Table 4. This is undoubtedly an asset of the present composite *ab initio* energy scheme. Note that, in deriving the above experimental value for ν_2 in ℓ-CCN^-, the photoelectron spectroscopic data of Garand *et al.*[39] were used (see peaks *A* and *a* therein) in combination with the revisited ℓ-$CCN(^2\Pi)$ $(000)\,\Pi_{1/2} - (010)\,\mu\Sigma$ energy splitting reported by Muzangwa and Reid[97]. As for c-$CNC^-(^1A_1)$, the vibrational band origins here computed with VPT2 and our composite force field are in reasonable agreement with those reported from the CcCR QFF[40]; see Table 5. The largest discrepancy (of up to $\sim$ 4 cm^{-1}) is found for the C−N asymmetric stretch (ν_3), a trend that becomes already clear at the harmonic level (ω_3), hence being probably better explained by the observed variance of the corresponding diagonal quadratic force constant F_{33} (Table 1). As noted previously, such disparities are undoubtedly attributed to the HO corrections [Eq. (12)]. Our best estimates place the fundamental band origins of c-$CNC^-(^1A_1)$ at 1460.3 (ν_1), 993.6 (ν_2), and 1046.4 cm^{-1} (ν_3). It is thus hoped that the results here presented aid in future high-resolution laboratory experiments and hopefully astronomical observations of C_2N^- as briefly surveyed

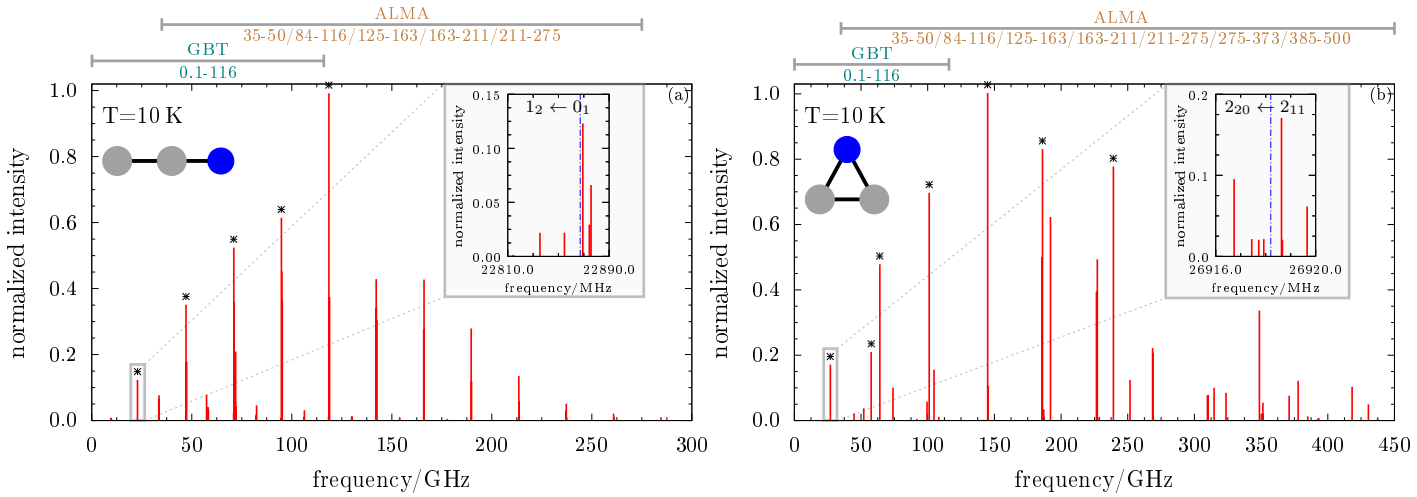

Fig. 4 Simulated rotational spectra at 10 K of (a). ℓ-CCN$^-$($^3\Sigma^-$) and (b). c-CNC$^-$($^1A_1$) in their ground vibrational states using PGOPHER[113] and the spectroscopic parameters presented in Tables 2, 3, and S5: these are A_0, B_0 and C_0 for the rotational constants and equilibrium values for the centrifugal distortion, fine and hyperfine parameters (see text). Working frequency ranges (in GHz) of the GBT and ALMA [from left to right: band 1 (both panels), and bands 3-6 (panel (a)) and bands 3-8 (panel (b))] are also displayed. The insets show the expected hyperfine splitting patterns for selected low-frequency transitions; blue dash-dotted lines highlight their positions without consideration of hyperfine couplings. Lines marked with '*' are listed in Table 7 in increasing order of their frequencies.

Table 7 Selected low-J (hyperfine) transitions of ℓ-CCN$^-$($^3\Sigma^-$) and c-CNC$^-$($^1A_1$) in their ground vibrational states and their expected uncertainties; see the marked lines in Figure 4. The corresponding instruments capable of detecting them are also surveyed.

ℓ-CCN$^-$($^3\Sigma^-$)			
Transition[a] $N'_{J'}(F') \leftarrow N''_{J''}(F'')$	Frequency (MHz)	Uncertainty[b] (MHz)	Instrument[c]
$1_2(3) \leftarrow 0_1(2)$	22869	15	GBT
$2_3(4) \leftarrow 1_2(3)$	47082	29	ALMA band 1/GBT
$3_4(5) \leftarrow 2_3(4)$	70961	44	GBT
$4_5(6) \leftarrow 3_4(5)$	94754	58	ALMA band 3/GBT
$5_6(7) \leftarrow 4_5(6)$	118514	73	
c-CNC$^-$($^1A_1$)			
Transition[a] $J'_{K'_a K'_c}(F') \leftarrow J''_{K''_a K''_c}(F'')$	Frequency (MHz)	Uncertainty[b] (MHz)	Instrument[c]
$2_{20}(3) \leftarrow 2_{11}(3)$	26919	17	GBT
$2_{11}(3) \leftarrow 2_{02}(3)$	57621	36	GBT
$1_{11}(2) \leftarrow 0_{00}(1)$	64028	40	GBT
$2_{02}(3) \leftarrow 1_{11}(2)$	101135	63	ALMA band 3/GBT
$3_{13}(4) \leftarrow 2_{02}(3)$	144956	90	ALMA band 4
$4_{04}(4) \leftarrow 3_{13}(3)$	185944	115	ALMA band 5
$3_{31}(4) \leftarrow 2_{20}(3)$	239192	148	ALMA band 6

[a] Only the most intense hyperfine components are reported.
[b] Estimated uncertainties in the predicted transition frequencies. The calculations assume that the theoretical A_0, B_0 and C_0 constants are accurate to within 0.062% (on average) of experiment (Table S3) so that their computed errors are $\Delta A_0 \approx \varepsilon A_0$, $\Delta B_0 \approx \varepsilon B_0$ and $\Delta C_0 \approx \varepsilon C_0$ with $\varepsilon = 6.2 \times 10^{-4}$. For ℓ-CCN$^-$, the calculated uncertainties in the transition frequencies are $\approx 2N' \Delta B_0$ (see text and Ref. 115), while for c-CNC$^-$ they are estimated using ΔA_0, ΔB_0 and ΔC_0 and the energy formulae given in Table 7.7 (page 245) of Ref. 95.
[c] ALMA band 1 is still under construction.

next.

4 Astrophysical implications

Figure 4 shows the simulated rotational spectra of ℓ-CCN$^-$($^3\Sigma^-$) and c-CNC$^-$($^1A_1$) at 10 K using PGOPHER[113] and the spectroscopic constants presented in Tables 2, 3, and S5; the parameters utilized here are A_0, B_0 and C_0 for the rotational constants, while the equilibrium values of the centrifugal distortion, fine and hyperfine structure are employed throughout, hence neglecting their reportedly very small vibrational ZPE effects[104,105,116]. Such a low rotational excitation temperature is typical of those found in cold dense cloud cores like TMC-1; the corresponding synthetic spectra obtained at higher T's characteristic of outer circumstellar envelopes of IRC+10216, $\approx$100 K, are depicted in Figure S2. Also displayed for comparison are the associated working ranges of GBT and ALMA receiver bands on top. A few selected low-J intense lines and their expected uncertainties are reported in Table 7, wherein a direct link between the predicted rotational signatures and the instrument detection capabilities is also made; the associated PGOPHER files can be found in the ESI.

As Figure 4 (a) evinces, the rotational spectrum of ℓ-CCN$^-$ is characteristic of a linear $^3\Sigma$ species, where each rotational level (except the one with $N=0$) is split into F_1 ($J=N+1$), F_2 ($J=N$) and F_3 ($J=N-1$) fine structure components by the presence of the electron spin-spin (λ) and spin-rotation (γ) interactions[115]. Here, J and N are total angular momentum quantum numbers including and excluding electron spin, respectively; accurate energy formulae for such F spin-triplets in terms of J, N, λ and γ were given by Schlapp[115]. As noted elsewhere[117] and clearly perceived here, rotational transitions among F_1 components show greater line strengths than those within the F_2 or F_3 ladders; see marked lines in Figure 4 (a) and Table 7. Inclusion of hyperfine interactions via electron spin-nuclear spin (b_F, c), ^{14}N quadrupole (eQq), and nuclear spin-rotation (c_I) cause additional intricate splittings in the observed spectrum as the inset of Figure 4 (a) portrays. These characteristic spectral signatures arising from its intrinsic (hyper)fine structure may indeed offer an extra diagnostic tool to identify this species, notably in radioastronomical

line surveys conducted at conceivably congested frequency domains like in the centimeter/millimeter-wave region (3-300 GHz). Note that, for simplicity, in Table 7, only the most intense hyperfine sub-component F_1 transitions are reported; the corresponding lower and upper states are identified by their total angular momentum quantum numbers including nuclear spin, F'' and F'. To further assess the reliability of our theoretical predictions for ℓ-CCN$^-$($^3\Sigma^-$), we again resort to the isoelectronic ℓ-CCO($^3\Sigma^-$) species. Using its spectroscopic constants calculated by the methods described here (sections 2.3 and 3), the corresponding synthetic rotational spectrum at 10 K has been so generated and compared with the simulated experimental one; see Figure S3. The results have shown that our approach is capable of reproducing the well-known interstellar ℓ-CCO lines $1_2 \leftarrow 0_1$ (22258.2 MHz) and $2_3 \leftarrow 1_2$ (45826.7 MHz) detected in TMC-1[117] to within 17 and 33 MHz of experiment, respectively, hence posing reliable constraints on the expected errors for C_2N^-; see Table 7. Such an accuracy should be sufficient to initiate astronomical line surveys on this nitrile anion, even when within the uncertainty range other and possibly unassigned transitions are found. Of course, because the uncertainties in the theoretically predicted line frequencies scale roughly as $\sim 2N'\Delta B_0$ [ΔB_0 is the error in the computed rotational constant (Table 7)], one would expect to find the least deviations in the low-N (low-frequency) range of the spectrum, *i.e.*, in the centimeter and lower end of the millimeter-wave regions ($\lesssim$150 GHz). Note, however, that, despite influencing the predicted (low-resolution) peak positions, such uncertainties are expected to have little effect on the overall hyperfine splitting patterns reported herein.

As for the c-CNC$^-$ asymmetric top, the predicted spectral distribution at 10 K and its most intense lines all fall within the centimeter/millimeter-wave range, hence being likewise amenable to radio observations; see Figure 4 (b). Owing to the intrinsic nature of its dipole moment (μ lies in the b principal axis which in turn coincides with C_2), the pure rotational spectrum of c-CNC$^-$ is characterized by b-type transitions for which $\Delta K_a = \pm 1$ and $\Delta K_c = \pm 1$ – the quantum numbers K_a and K_c refer to the projection of J along the molecules' figure axis in the prolate and oblate limits, respectively. Moreover, because the two equivalent off-axis C atoms are bosons, only half of the rotational levels exist, those with K_a+K_c even. As Figure 4 (b) and Table 7 show, the most intense lines of such occur in the Q- and R-branches[96]. Inclusion of hyperfine ^{14}N quadrupole and spin-rotation couplings have the expected effects on the observed spectrum, with the predicted splitting pattern for the lowest frequency intense transition $2_{20} \leftarrow 2_{11}$ being shown in the inset of Figure 4 (b). Again, such intrinsic (hyper)fine structure undoubtedly convey an additional identity to the underlying species that might be extremely useful to circumvent spectral line confusion, hence enabling its unambiguous identification in space.

Apart from the likely detectability of ℓ-CCN$^-$ and c-CNC$^-$ in the radio band with GBT, ALMA, and, possibly, 4GREAT (onboard the Stratospheric Observatory for Infrared Astronomy, SOFIA) at higher excitation T's (Figure S2), astronomical searches in the mid-/long-infrared (IR) should also reveal, if abundant, these molecules' rovibrational signatures. Indeed, their predicted band origins (Tables 4 and 5) are within the instrument ranges of the Echelon-Cross-Echelle Spectrograph (EXES) onboard the SOFIA ($\approx$2200–350 cm^{-1}) as well as MIRI, the Mid-InfraRed Instrument for the James Webb Space Telescope (JWST) to be launched later this year. The present study and the highly accurate theoretical data supplied herein will certainly assist in such spectral surveys, thus paving the way for their unequivocal identification both in the laboratory and in space.

Apart from the main isotopologues, the data presented herein for the singly-substituted ^{13}C- or ^{15}N-bearing variants and their intrinsic (mass-shifted) spectral signatures (including hyperfine structure) add considerably to our C_2N^- observational tool kit. These species could significantly contribute to the spectral richness of line surveys and their eventual detection would undoubtedly convey additional information on C_2N^- formation pathways and chemical fractionation effects[114], as well as help in gaining extra knowledge on the physical conditions (densities, temperatures and timescales) characteristic of the environment in which they form; this is the case for the recently identified rare isotopologues of complex organic molecules[118].

5 Conclusions

Observations of large, highly-dipolar carbon chain anions in a variety of interstellar environments have helped in establishing the grounds on which our current knowledge of ISM anion chemistry is based. The question remains as to whether the smallest congeners indeed play a role and, if so, how they are formed[29,30,33,34,36]. Studying the astronomical abundance of even smaller anions, *e.g.*, C_2^-, CH^-, C_2H^-, CN^-, and C_2N^-, for which REA to their parent neutrals appears to be an unlikely formation pathway, should then help in providing the answers. Advancing this research undoubtedly requires accurate knowledge of their spectroscopic signatures, which for the case of C_2N^- are as yet largely absent. Prompted by such a pursuit and by the recent experimental findings by Chacko *et al.*[36], in this work, we provide such data for both ground ℓ-CCN$^-$($^3\Sigma^-$) and low-lying c-CNC$^-$($^1A_1$) forms using state-of-the-art rovibrational quantum chemical techniques. Special efforts are put into the computation of their QFFs by means of a high-level CC-based composite energy scheme that includes extrapolations to both (all-electron) one-particle and (approximate) $\mathscr{N}$-particle basis set limits, in addition to relativistic effects. The final analytic QFFs were then obtained in the usual fashion by least-squares fit, affording composite equilibrium geometries and final force constants with unprecedented accuracy. With these PESs, nuclear motion calculations have then been carried out using both perturbation theory and exact variational methods. Besides standard rovibrational spectroscopic constants and anharmonic vibrational frequencies, the computed data set of properties includes fine and hyperfine interaction constants evaluated *ab initio* at the QFF equilibrium geometries and is expected to embrace the most reliable theoretical estimates to date for C_2N^-; similar attributes are also provided for the ^{13}C and ^{15}N singly-substituted isotopologues. The spectroscopic parameters so found can be readily introduced as guesses in standard experimental data reduction analyses through effective Hamiltonians. On the basis of benchmark calculations per-

formed anew for a minimal test set of prototypical triatomics, the present protocol is shown to rival well-established methodologies currently available in the literature, producing rotational constants and vibrational fundamentals to within $\sim 0.1\%$ and $\sim 0.3\%$ of experiment, respectively, for species with at least two heavy atoms. This preliminary assessment thus allows for a systematic evaluation of the expected uncertainties for C_2N^-. By relying on their presumably similar electronic structure, comparisons are particularly made with the isoelectronic ℓ-CCO($^3\Sigma^-$) radical for which accurate gas-phase experimental data are available. Specifically for ℓ-CCN$^-$($^3\Sigma^-$), the calculated ν_2 bending frequency is shown to reproduce its associated experimental estimate to better than $1\,\mathrm{cm}^{-1}$. Such accuracies reported herein should be sufficient for astronomical line surveys on C_2N^-. Using the theoretically-predicted spectroscopic constants, the rotational spectra of both ℓ-CCN$^-$($^3\Sigma^-$) and c-CNC$^-$($^1A_1$) are derived and the predicted transitions frequencies are further compared with working frequency ranges of powerful astronomical facilities such as GBT and ALMA. Our best theoretical estimate places c-CNC$^-$($^1A_1$) at about $15.3\,\mathrm{kcal\,mol}^{-1}$ above ℓ-CCN$^-$($^3\Sigma^-$) which might limit its (astro-)chemical synthesis to higher-temperature environments such as in circumstellar envelopes of evolved stars and in the atmosphere of Titan.

Conflicts of interest

There are no conflicts to declare.

Acknowledgements

This work has received funding from the European Union's Horizon 2020 research and innovation program under the Marie Sklodowska-Curie grant agreement No 894321. C.M.R.R thanks also the Academic Leiden Interdisciplinary Cluster Environment (ALICE) provided by Leiden University for the computational resources.

References

1 A. Dalgarno and R. A. McCray, *ApJ*, 1973, **181**, 95–100.
2 P. Sarre, *J. Chim. Phys.*, 1980, **77**, 769–771.
3 E. Herbst, *Nature*, 1981, **289**, 656–657.
4 B. A. McGuire, *ApJS*, 2018, **239**, 17.
5 P. M. Solomon and W. Klemperer, *ApJ*, 1972, **178**, 389–422.
6 W. D. Watson and E. E. Salpeter, *ApJ*, 1972, **174**, 321–340.
7 W. D. Watson and E. E. Salpeter, *ApJ*, 1972, **175**, 659–671.
8 E. Herbst and W. Klemperer, *ApJ*, 1973, **185**, 505–534.
9 A. Dalgarno and J. H. Black, *Rep. Prog. Phys.*, 1976, **39**, 573–612.
10 Y. Morisawa, H. Hoshina, Y. Kato, Z. Simizu, S. Kuma, N. Sogoshi, M. Fushitani, S. Watanabe, Y. Miyamoto, T. Momose, Y. Kasai and K. Kawaguchi, *PASJ*, 2005, **57**, 325–334.
11 M. C. McCarthy, C. A. Gottlieb, H. Gupta and P. Thaddeus, *Astrophys. J.*, 2006, **652**, L141–L144.
12 J. Simons, *J. Phys. Chem. A*, 2008, **112**, 6401–6511.
13 M. Larsson, W. D. Geppert and G. Nyman, *Rep. Prog. Phys.*, 2012, **75**, 066901.
14 R. C. Fortenberry, *J. Phys. Chem. A*, 2015, **119**, 9941–9953.
15 T. J. Millar, C. Walsh and T. A. Field, *Chem. Rev.*, 2017, **117**, 1765–1795.
16 Cernicharo, J., Marcelino, N., Pardo, J. R., Agúndez, M., Tercero, B., de Vicente, P., Cabezas, C. and Bermúdez, C., *A&A*, 2020, **641**, L9.
17 R. P. A. Bettens and E. Herbst, *ApJ*, 1996, **468**, 686–693.
18 S. Petrie and E. Herbst, *ApJ*, 1997, **491**, 210–215.
19 R. Terzieva and E. Herbst, *Int. J. Mass Spectrom.*, 2000, **201**, 135–142.
20 T. J. Millar, E. Herbst and R. P. A. Bettens, *MNRAS*, 2000, **316**, 195–203.
21 T. J. Millar, C. Walsh, M. A. Cordiner, R. N. Chuimín and E. Herbst, *ApJ*, 2007, **662**, L87–L90.
22 E. Herbst and Y. Osamura, *ApJ*, 2008, **679**, 1670–1679.
23 C. Walsh, N. Harada, E. Herbst and T. J. Millar, *ApJ*, 2009, **700**, 752–761.
24 F. Güthe, M. Tulej, M. V. Pachkov and J. P. Maier, *ApJ*, 2001, **555**, 466–471.
25 F. Carelli, M. Satta, T. Grassi and F. A. Gianturco, *ApJ*, 2013, **774**, 97.
26 F. Carelli, F. A. Gianturco, R. Wester and M. Satta, *J. Chem. Phys.*, 2014, **141**, 054302.
27 C. Desfrancois, H. Abdoul-Carmine and J. P. Schermann, *Int. J. Mod. Phys. B*, 1996, **10**, 1339–1395.
28 M. Tulej, D. A. Kirkwood, M. Pachkov and J. P. Maier, *ApJ*, 1998, **506**, L69–L73.
29 S. Petrie, *MNRAS*, 1996, **281**, 137–144.
30 M. A. Cordiner and T. J. Millar, *ApJ*, 2009, **697**, 68–78.
31 Agúndez, M., Cernicharo, J., Guélin, M., Kahane, C., Roueff, E., Klos, J., Aoiz, F. J., Lique, F., Marcelino, N., Goicoechea, J. R., González García, M., Gottlieb, C. A., McCarthy, M. C. and Thaddeus, P., *A&A*, 2010, **517**, L2.
32 M. A. Cordiner and S. B. Charnley, *ApJ*, 2012, **749**, 120.
33 F. A. Gianturco, M. Satta, E. Yurtsever and R. Wester, *ApJ*, 2017, **850**, 42.
34 E. Yurtsever, M. Satta, R. Wester and F. A. Gianturco, *J. Phys. Chem. A*, 2020, **124**, 5098–5108.
35 B. Eichelberger, T. P. Snow, C. Barckholtz and V. M. Bierbaum, *ApJ*, 2007, **667**, 1283–1289.
36 R. Chacko, S. Banhatti, M. Nrisimhamurty, J. K. Yadav, A. K. Gupta and G. Aravind, *ApJ*, 2020, **905**, 90.
37 M. Nakajima, *J. Mol. Spectrosc.*, 2017, **331**, 106–108.
38 G. Pascoli and H. Lavendy, *Chem. Phys. Lett.*, 1999, **312**, 333–340.
39 E. Garand, T. I. Yacovitch and D. M. Neumark, *J. Chem. Phys.*, 2009, **130**, 064304.
40 R. C. Fortenberry, T. J. Lee and X. Huang, *Phys. Chem. Chem. Phys.*, 2017, **19**, 22860–22869.
41 J. Franz, B. P. Mant, L. González-Sánchez, R. Wester and F. A. Gianturco, *J. Chem. Phys.*, 2020, **152**, 234303.
42 J. K. Anderson and L. M. Ziurys, *Astrophys. J.*, 2014, **795**, L1.
43 J. Grant Hill, A. Mitrushchenkov, K. E. Yousaf and K. A. Pe-

terson, *J. Chem. Phys.*, 2011, **135**, 144309.
44 A. M. Mebel and R. I. Kaiser, *ApJ*, 2002, **564**, 787–791.
45 M. C. McCarthy, K. L. K. Lee, R. A. Loomis, A. M. Burkhardt, C. N. Shingledecker, S. B. Charnley, M. A. Cordiner, E. Herbst, S. Kalenskii, E. R. Willis, C. Xue, A. J. Remijan and B. A. McGuire, *Nat. Astron.*, 2021, **5**, 176–180.
46 D. S. N. Parker and R. I. Kaiser, *Chem. Soc. Rev.*, 2017, **46**, 452–463.
47 S. A. Sandford, M. Nuevo, P. P. Bera and T. J. Lee, *Chem. Rev.*, 2020, **120**, 4616–4659.
48 V. Vuitton, P. Lavvas, R. Yelle, M. Galand, A. Wellbrock, G. Lewis, A. Coates and J.-E. Wahlund, *P&SS*, 2009, **57**, 1558–1572.
49 M. S. Schuurman, W. D. Allen and H. F. Schaefer III, *J. Comp. Chem.*, 2005, **26**, 1106–1112.
50 X. Huang and T. J. Lee, *J. Chem. Phys.*, 2008, **129**, 044312.
51 X. Huang and T. J. Lee, *J. Chem. Phys.*, 2009, **131**, 104301.
52 R. C. Fortenberry, T. J. Lee and H. S. Müller, *Mol. Astrophys.*, 2015, **1**, 13–19.
53 W. J. Morgan, D. A. Matthews, M. Ringholm, J. Agarwal, J. Z. Gong, K. Ruud, W. D. Allen, J. F. Stanton and H. F. Schaefer, *J. Chem. Theory Comput.*, 2018, **14**, 1333–1350.
54 C. M. R. Rocha, *Proc. Int. Astron. Union*, 2019, **15**, 61–64.
55 A. G. Császár, *WIREs Computational Molecular Science*, 2012, **2**, 273–289.
56 H. H. Nielsen, *Rev. Mod. Phys.*, 1951, **23**, 90–136.
57 I. M. Mills, *Molecular Spectroscopy: Modern Research*, Academic Press, New York, 1972, ch. 3, pp. 115–140.
58 M. Aliev and J. Watson, *Molecular Spectroscopy: Modern Research*, Academic Press, New York, 1985, ch. 1, pp. 1–67.
59 J. Tennyson, M. A. Kostin, P. Barletta, G. J. Harris, O. L. Polyansky, J. Ramanlal and N. F. Zobov, *Comput. Phys. Commun.*, 2004, **163**, 85–116.
60 J. F. Gaw, A. Willets, W. H. Green and N. C. Handy, *SPECTRO, A Theoretical Spectroscopy Package, Version 3.0*, 1996.
61 A. R. Hoy, I. M. Mills and G. Strey, *Mol. Phys.*, 1972, **24**, 1265–1290.
62 A. J. C. Varandas, *Annu. Rev. Chem.*, 2018, **69**, 177–203.
63 K. Raghavachari, G. W. Trucks, J. A. Pople and M. Head-Gordon, *Chem. Phys. Let.*, 1989, **157**, 479–483.
64 D. Peng and M. Reiher, *Theor. Chem. Acc.*, 2012, **131**, 1081.
65 P. J. Knowles, C. Hampel and H. Werner, *J. Chem. Phys.*, 1993, **99**, 5219–5227.
66 J. D. Watts, J. Gauss and R. J. Bartlett, *J. Chem. Phys.*, 1993, **98**, 8718–8733.
67 T. H. Dunning, *J. Chem. Phys.*, 1989, **90**, 1007–1023.
68 R. A. Kendall, T. H. Dunning and R. J. Harrison, *J. Chem. Phys.*, 1992, **96**, 6796–6806.
69 D. E. Woon and T. H. Dunning, *J. Chem. Phys.*, 1995, **103**, 4572–4585.
70 H.-J. Werner, P. J. Knowles, G. Knizia, F. R. Manby, M. Schütz *et al.*, *MOLPRO, version 2020.1, A Package of* Ab Initio *Programs*, see: http://www.molpro.net.
71 D. Feller, *J. Chem. Phys.*, 1993, **98**, 7059–7071.
72 A. J. C. Varandas, *J. Chem. Phys.*, 2007, **126**, 244105–244119.
73 M. Douglas and N. M. Kroll, *Ann. Phys.*, 1974, **82**, 89–155.
74 G. Jansen and B. A. Hess, *Phys. Rev. A*, 1989, **39**, 6016–6017.
75 W. A. de Jong, R. J. Harrison and D. A. Dixon, *J. Chem. Phys.*, 2001, **114**, 48–53.
76 D. Feller, K. A. Peterson and T. D. Crawford, *J. Chem. Phys.*, 2006, **124**, 054107.
77 D. Feller, K. A. Peterson and D. A. Dixon, *J. Chem. Phys.*, 2008, **129**, 204105.
78 J. Noga and R. J. Bartlett, *J. Chem. Phys.*, 1987, **86**, 7041–7050.
79 G. E. Scuseria and H. F. Schaefer, *Chem. Phys. Lett.*, 1988, **152**, 382–386.
80 S. A. Kucharski and R. J. Bartlett, *J. Chem. Phys.*, 1992, **97**, 4282–4288.
81 N. Oliphant and L. Adamowicz, *J. Chem. Phys.*, 1991, **94**, 1229–1235.
82 A. Tajti, P. G. Szalay, A. G. Császár, M. Kállay, J. Gauss, E. F. Valeev, B. A. Flowers, J. Vázquez and J. F. Stanton, *J. Chem. Phys.*, 2004, **121**, 11599–11613.
83 A. Karton and J. M. L. Martin, *J. Chem. Phys.*, 2010, **133**, 144102.
84 W. J. Morgan, X. Huang, I. Schaefer, Henry F and T. J. Lee, *MNRAS*, 2018, **480**, 3483–3490.
85 A. Karton, *J. Chem. Phys.*, 2020, **153**, 024102.
86 C. Puzzarini and V. Barone, *Phys. Chem. Chem. Phys.*, 2020, **22**, 6507–6523.
87 D. Z. Goodson, *J. Chem. Phys.*, 2002, **116**, 6948–6956.
88 M. Kállay and J. Gauss, *J. Chem. Phys.*, 2005, **123**, 214105.
89 M. Kállay, P. R. Nagy, D. Mestera, Z. Rolik, G. Samu, J. Csontos, J. Csóka, P. B. Szabó, L. Gyevi-Nagy, B. Hégely, I. Ladjánszki, L. Szegedy, B. Ladóczki, K. Petrov, M. Farkas, P. D. Mezei and A. Ganyecz, *MRCC, A Quantum Chemical Program Suite*, see: http://www.mrcc.hu.
90 C. E. Dateo, T. J. Lee and D. W. Schwenke, *J. Chem. Phys.*, 1994, **101**, 5853–5859.
91 R. C. Fortenberry, X. Huang, A. Yachmenev, W. Thiel and T. J. Lee, *Chem. Phys. Lett.*, 2013, **574**, 1–12.
92 M. B. Gardner, B. R. Westbrook, R. C. Fortenberry and T. J. Lee, *Spectrochim. Acta A Mol. Biomol. Spectrosc.*, 2021, **248**, 119184.
93 E. K. Conway, I. E. Gordon, O. L. Polyansky and J. Tennyson, *J. Chem. Phys.*, 2020, **152**, 024105.
94 J. R. Reimers, L. K. McKemmish, R. H. McKenzie and N. S. Hush, *Phys. Chem. Chem. Phys.*, 2015, **17**, 24641–24665.
95 W. Gordy and R. L. Cook, *Microwave Molecular Spectra: Technique of Organic Chemistry*, John Wiley & Sons, New York, 2nd edn, 1984, vol. 9.
96 S. A. Cooke and P. Ohring, *J. Spectrosc.*, 2013, **2013**, 698392.
97 L. Muzangwa and S. A. Reid, *J. Mol. Spectrosc.*, 2015, **310**, 105–108.

98 C. Puzzarini, J. F. Stanton and J. Gauss, *Int. Rev. Phys. Chem.*, 2010, **29**, 273–367.
99 O. Vahtras, O. Loboda, B. Minaev, H. Ågren and K. Ruud, *Chem. Phys.*, 2002, **279**, 133–142.
100 G. Tarczay, P. G. Szalay and J. Gauss, *J. Phys. Chem. A*, 2010, **114**, 9246–9252.
101 R. F. Curl, *Mol. Phys.*, 1965, **9**, 585–597.
102 M. Engström, B. Minaev, O. Vahtras and H. Ågren, *Chem. Phys.*, 1998, **237**, 149–158.
103 K. Aidas, C. Angeli, K. L. Bak, V. Bakken, R. Bast, L. Boman *et al.*, *DALTON, A Molecular Electronic Structure Program, Release Dalton2021.alpha (2020)*, see: http://daltonprogram.org.
104 Z. Abusara, M. Dehghani and N. Moazzen-Ahmadi, *Chem. Phys. Lett.*, 2006, **417**, 206–210.
105 G. Cazzoli, V. Lattanzi, T. Kirsch, J. Gauss, B. Tercero, J. Cernicharo and C. Puzzarini, *A&A*, 2016, **591**, A126.
106 P. Pyykkö, *Mol. Phys.*, 2018, **116**, 1328–1338.
107 J. M. Lehn and J. P. Kintzinger, in *Nitrogen-14 Nuclear Quadrupole Effects*, ed. M. Witanowski and G. A. Webb, Springer US, Boston, MA, 1973, pp. 79–161.
108 A. Aerts and A. Brown, *J. Chem. Phys.*, 2019, **150**, 224302.
109 H. Linnartz, T. Motylewski, F. Maiwald, D. Roth, F. Lewen, I. Pak and G. Winnewisser, *Chem. Phys. Lett.*, 1998, **292**, 188–192.
110 C. A. Gottlieb, S. Brünken, M. C. McCarthy and P. Thaddeus, *J. Chem. Phys.*, 2007, **126**, 191101.
111 P. Thaddeus, C. A. Gottlieb, H. Gupta, S. Brünken, M. C. McCarthy, M. Agúndez, M. Guélin and J. Cernicharo, *ApJ*, 2008, **677**, 1132–1139.
112 J. A. J. Fitzpatrick, F. R. Manby and C. M. Western, *J. Chem. Phys.*, 2005, **122**, 084312.
113 C. M. Western, *J. Quant. Spectrosc. Radiat. Transf.*, 2017, **186**, 221–242.
114 C. M. R. Rocha and H. Linnartz, *A&A*, 2021, **647**, A142.
115 R. Schlapp, *Phys. Rev.*, 1937, **51**, 342–345.
116 D. Zhao, K. D. Doney and H. Linnartz, *ApJ*, 2014, **791**, L28.
117 M. Ohishi, H. Suzuki, S.-I. Ishikawa, C. Yamada, H. Kanamori, W. M. Irvine, R. D. Brown, P. D. Godfrey and N. Kaifu, *ApJL*, 1991, **380**, L39.
118 D. E. Woon, *The Astrochymist*, `http://astrochymist.org/astrochymist_isotopologues.html`.